


Article

CeO₂-Promoted PtSn/SiO₂ as a High-Performance Catalyst for the Oxidative Dehydrogenation of Propane with Carbon Dioxide

Li Wang, Guo-Qing Yang, Xing Ren and Zhong-Wen Liu * 

Key Laboratory of Syngas Conversion of Shaanxi Province, School of Chemistry & Chemical Engineering, Shaanxi Normal University, Xi'an 710119, China; kingli@snnu.edu.cn (L.W.); gqyang@snnu.edu.cn (G.-Q.Y.); rxqnmhhh@snnu.edu.cn (X.R.)

* Correspondence: zwliu@snnu.edu.cn

Abstract: The oxidative dehydrogenation of propane with CO₂ (CO₂-ODP) has been extensively investigated as a promising green technology for the efficient production of propylene, but the lack of a high-performance catalyst is still one of the main challenges for its industrial application. In this work, an efficient catalyst for CO₂-ODP was developed by adding CeO₂ to PtSn/SiO₂ as a promoter via the simple impregnation method. Reaction results indicate that the addition of CeO₂ significantly improved the catalytic activity and propylene selectivity of the PtSn/SiO₂ catalyst, and the highest space-time yield of 1.75 g(C₃H₆)·g(catalyst)⁻¹·h⁻¹ was achieved over PtSn/SiO₂ with a Ce loading of 6 wt%. The correlation of the reaction results with the characterization data reveals that the introduction of CeO₂ into PtSn/SiO₂ not only improved the Pt dispersion but also regulated the interaction between Pt and Sn species. Thus, the essential reason for the promotional effect of CeO₂ on CO₂-ODP performance was rationally ascribed to the enhanced adsorption of propane and CO₂ originating from the rich oxygen defects of CeO₂. These important understandings are applicable in further screening of promoters for the development of a high-performance Pt-based catalyst for CO₂-ODP.

Keywords: oxidative dehydrogenation; propane; carbon dioxide; supported PtSn catalyst; ceria



Citation: Wang, L.; Yang, G.-Q.; Ren, X.; Liu, Z.-W. CeO₂-Promoted PtSn/SiO₂ as a High-Performance Catalyst for the Oxidative Dehydrogenation of Propane with Carbon Dioxide. *Nanomaterials* **2022**, *12*, 417. <https://doi.org/10.3390/nano12030417>

Academic Editors: Anna Maria Venezia and Giorgio Vilardi

Received: 25 December 2021

Accepted: 25 January 2022

Published: 27 January 2022

Publisher's Note: MDPI stays neutral with regard to jurisdictional claims in published maps and institutional affiliations.



Copyright: © 2022 by the authors. Licensee MDPI, Basel, Switzerland. This article is an open access article distributed under the terms and conditions of the Creative Commons Attribution (CC BY) license (<https://creativecommons.org/licenses/by/4.0/>).

1. Introduction

Propylene is one of the most important raw materials for the chemical industry [1,2]. It is mainly produced by the steam cracking of naphtha and the byproduct of fluid catalytic cracking (FCC) of heavier oil fractions, which suffer from both low propylene yield and high energy consumption [3]. Moreover, these technologies cannot meet the continuously increased market demand for propylene. As a consequence and owing to the growing alternative supply of propane from the shale gas, the catalytically direct dehydrogenation of propane to propylene (PDH) has been attracting increased attention. However, the currently industrialized PDH process is still challenged by the quick deactivation of commercial PtSn/Al₂O₃ or CrO_x/Al₂O₃ catalysts, low yields of propylene limited by thermodynamics, and high reaction temperatures [4,5]. To address these issues, the oxidative dehydrogenation of propane to propylene using O₂, CO₂, N₂O, or SO_x as an oxidant is proposed as a more efficient route [6,7]. Among these alternative processes, the oxidative dehydrogenation of propane with greenhouse gas of CO₂ (CO₂-ODP) is the most attractive from an environmental viewpoint. On the one hand, in comparison with PDH, CO₂-ODP can effectively enhance the equilibrium conversion of propane by removing the produced hydrogen [4,8]. On the other hand, a higher selectivity of propylene for CO₂-ODP can be achieved in comparison with that achieved by using O₂ as an oxidant, for which deep oxidation is an important issue. Moreover, the CO₂-ODP process provides an attractively tandem approach via efficient production of propylene with simultaneous conversion of CO₂ to

CO [9,10]. Currently, a number of catalysts that predominantly contain supported metal oxides, e.g., Cr, V, In, Ga, and Zn, have been extensively investigated for CO₂-ODP [4,11]. However, mechanistic understanding of the simultaneous activation of the C=O bonds in CO₂ molecules and C-H bonds with the inhibited breaking of C-C bonds in propane molecules is very limited, which impedes the rational design of an efficient catalyst for CO₂-ODP. Thus, a green CO₂-ODP process is still far from industrial application. In fact, under industrially relevant reaction temperatures, C₃H₈ can react with CO₂ via two distinct reaction routes, i.e., CO₂-ODP (CO₂ + C₃H₈ → C₃H₆ + CO + H₂O) and the reforming of propane with CO₂ (CO₂-RP, 3CO₂ + C₃H₈ → 6CO + 4H₂) [12,13]. Moreover, the extents of the two reactions are kinetically determined by the employed catalyst. Generally, metal-oxide catalysts, such as VO_x and CrO_x are favorable for selectively breaking C-H bonds in propane to produce propylene, but they are less active for activation of CO₂ molecules [14,15]. In contrast, the supported metals, such as Pt/CeO₂ and Pd/CeZrAlO_x, are good catalysts for the production of synthesis gas via the CO₂-RP reaction, in which the selective splitting of C-C bonds in propane is favored, with the simultaneous activation of C=O bonds in CO₂ [13,16]. Thus, as a result of the competing nature of the CO₂-ODP and CO₂-RP reactions, the favorable activation of C-H bonds with the inhibited breaking of C-C bonds in propane is one of the key requirements for development of a high-performance CO₂-ODP catalyst.

In fact, contrary to Pt/CeO₂, with a greater ability to break C-C bonds in alkane molecules, supported PtSn has already been applied as a commercial catalyst for the PDH reaction [17]. This rigorously indicates that the addition of SnO₂ into Pt shifts the selective breaking of C-C bonds to the favorable activation of C-H bonds in propane molecules. Although the action nature of the added SnO₂ on Pt is still not unambiguously revealed, the improved Pt dispersion and the electron transfer between Pt and Sn species are commonly agreed to be key factors in determining the activity and selectivity of propene for the PDH reaction [18,19]. This is further supported by quantitative studies on the interactions between Pt and Sn species, which can be tuned by adding promoters and changing the synthesis methods of the catalyst, including thermal treatment under different atmospheres [20].

In the case of CO₂ activation, CeO₂ with a high oxygen-storage capacity and abundant oxygen defects was extensively investigated as a support/promoter/catalyst for the reactions involving CO₂ as a reactant [21]. In our previous study [22], CeO₂ and CeO₂-based solid solutions were found to be effective for converting CO₂ into CO during the oxidative dehydrogenation of ethylbenzene with CO₂, the ability of which is closely connected with oxygen defects over the oxides. Moreover, two functions of CeO₂ as an additive over Pt-based catalysts for the PDH reaction were manifested as stabilizing Pt, suppressing coke deposition [23].

Based on these analyses, the combination of PtSn with CeO₂ may create a good CO₂-ODP catalyst, provided that the assisted activation of CO₂ is achieved by oxygen defects over CeO₂. Moreover, silica is widely used as a support for the CO₂-ODP reaction [6], the side reactions of which are inhibited in comparison with Al₂O₃ with a higher acidity [24,25]. Thus, in this work, a high-performance CO₂-ODP catalyst was developed by simply impregnating the CeO₂ precursor into PtSn/SiO₂. The PtSn/SiO₂ catalyst, with a Ce loading of 6 wt%, showed a space-time yield of propene as high as 1.75 g(C₃H₆)·g(catalyst)⁻¹·h⁻¹ and superior stability, outperforming the state-of-the-art catalysts, including the supported oxides, such as CrO_x, GaO_x, and VO_x, as well as the supported metals, such as Pd and Fe₃Ni. The essence of the high CO₂-ODP performance of CeO₂-promoted PtSn/SiO₂ is rigorously revealed as the enhanced adsorption of propane and CO₂, which favors the selective breaking of C-H bonds in propane with the expedited tandem conversion of CO₂ to CO.

2. Experimental

2.1. Catalyst Preparation

PtSnCe/SiO₂, PtCe/SiO₂, PtSn/SiO₂, and SnCe/SiO₂ catalysts were prepared by the sequential impregnation method, whereby the amounts of Pt, Sn, and Ce were fixed at 0.5, 0.9, and 6 wt%, respectively. The reagents of H₂PtCl₆·6H₂O (Pt ≥ 37.5%, Shanghai Aladdin Biochemical Co., Ltd., Shanghai, China), SnCl₂·6H₂O (>99.9%, Guangdong Guanghua Sci-Tech Co., Ltd., Shantou, China), and Ce(NO₃)₃·6H₂O (>99.0%, Shanghai Macklin Biochemical Co., Ltd., Shanghai, China) were chosen as the precursors of the Pt, Sn, and Ce species, respectively. The SiO₂ support, with a specific BET surface area of 580 m²/g and an average pore diameter of 3.0 nm (Fuji Silysia Chemical Ltd., Kasugai Aichi, Japan), was pre-treated in air at 550 °C for 3 h. Impregnation was performed at 80 °C under stirring for 2 h, and the subsequent drying was carried out at 80 °C for 4 h. Following sequential impregnation with the desired amount of aqueous solution of H₂PtCl₆·6H₂O, the acetone solution of SnCl₂·2H₂O and the aqueous solution of Ce(NO₃)₃·6H₂O, PtSnCe/SiO₂, PtCe/SiO₂, PtSn/SiO₂, and SnCe/SiO₂ catalysts were obtained after calcining at 500 °C for 3 h under atmospheric conditions.

2.2. Catalyst Characterizations

N₂ physical adsorption/desorption isotherms were measured on a Bel-sorp-Max instrument at −196 °C. Before each experiment, the sample was degassed at 300 °C under vacuum for 10 h. Specific surface area and pore-size distribution (PSD) were calculated by the Brunauer–Emmett–Teller equation (BET) and Barrett–Joyner–Halenda method (BJH), respectively.

X-ray diffraction (XRD) patterns were recorded on an X-ray diffractometer (Bruker D8 Advance) equipped with Cu-Kα radiation (40 kV, 40 mA). The sample was scanned from the 2θ of 10 to 80° with a rate of 0.2 s/step.

Transmission electron microscopy (TEM) images were obtained with a high-resolution transmission electron microscope (Tecnai G2 F20, FEI) operated at 200 kV. Before measurement, the fresh sample was pre-reduced at 500 °C in 10 vol% H₂/Ar for 1 h. Then, about 2 mg of the reduced sample was ultrasonically dispersed in anhydrous ethanol (2 mL). After 1 h, two drops of the suspension were deposited on a carbon-enhanced copper grid and dried at 60 °C in air for 0.5 h.

H₂-O₂ titration experiments were carried out on a Micromeritics Autochem 2920 instrument to determine the dispersion of Pt. For each test, a total of 150 mg of the sample was pre-reduced at 500 °C for 1 h in 10 vol% H₂/Ar (30 mL/min). After cooling to 50 °C in Ar, a flow of 3 vol% O₂/Ar (30 mL/min) was pulsed until the consumption peaks became stable. Subsequently, the sample was purged under an Ar flow for 1 h, and consecutive pulses of 10 vol% H₂/Ar (0.50 mL) were performed. By assuming that the adsorption stoichiometry factor of Pt/H₂ equals to 2/3, according to references [26,27], the dispersion of Pt was calculated using the following Equation (1).

$$\text{Dispersion (\%)} = \frac{V_{\text{H}_2} \times f \times M_{\text{Pt}}}{W_{\text{Pt}} \times 22,414} \times 100 \quad (1)$$

where V_{H_2} is the volume of adsorbed H₂ (mL), f is the stoichiometry factor, M_{Pt} is the atomic weight of Pt (g/mol), and W_{Pt} is the weight of the supported Pt on the sample (g).

Experiments concerning temperature-programmed reduction of H₂ (H₂-TPR) were carried out on a Micromeritics Autochem 2920 instrument. About 100 mg of the sample was pre-treated at 350 °C for 0.5 h under an Ar stream. After cooling to 50 °C, H₂-TPR was performed from 50 to 800 °C at a heating rate of 10 °C/min under a 10 vol% H₂/Ar flow (30 mL/min). H₂ consumption was monitored and determined by a pre-calibrated thermal conductivity detector (TCD).

X-ray photoelectron spectroscopy (XPS) was conducted on an X-ray photoelectron spectrometer (KRATOS Analytical Ltd., Manchester, UK) equipped with an Al-Kα radiation source (1486.6 eV). Before measurements, all the samples were pre-reduced at 500 °C

for 1 h in 10 vol% H₂/Ar. The C 1s spectrum at 284.6 eV was applied to calibrate the binding energy.

Diffuse reflectance infrared Fourier transform spectroscopy (DRIFTS) of adsorbed CO (CO-DRIFTS) was carried out on a Nicolet iS50 instrument (Thermo Scientific) equipped with an in situ cell. Firstly, the sample was reduced in situ at 500 °C for 1 h in 10 vol% H₂/Ar with a flow rate of 30 mL/min. After this, the sample was cooled to 30 °C and purged with Ar. Then, 10 vol% CO/Ar with a flow rate of 30 mL/min was introduced in the cell for 0.5 h. Afterwards, the sample was purged with Ar to remove any physically adsorbed CO on the surface of sample, and DRIFTS spectra were recorded. Prior to each experiment, the background spectra were recorded.

Experiments concerning temperature-programmed desorption of C₃H₈/CO₂/C₃H₆ (C₃H₈/CO₂/C₃H₆-TPD) were performed on a Micromeritics Autochem 2920 instrument. About 100 mg of the sample was pre-reduced at 500 °C for 1 h in 10 vol% H₂/Ar. After this, the sample was cooled to 70 °C and purged with Ar. Then, the pre-treated sample was saturated with pure C₃H₈, CO₂, or C₃H₆ with a flow rate of 30 mL/min for 1 h. Afterwards, the sample was purged by an Ar stream for 1 h, and temperature-programmed desorption of C₃H₈/CO₂/C₃H₆ was performed from 70 to 600 °C at a heating rate of 10 °C/min, respectively. The amount of desorbed C₃H₈/CO₂/C₃H₆ was monitored and determined by a pre-calibrated thermal conductivity detector (TCD).

Thermogravimetric and differential scanning calorimetry analyses (TG-DSC) of the spent catalysts were carried out on a Q600SDT Thermoanalyzer System (TA Instruments). For each test, about 5 mg of the spent catalyst was heated from 50 to 800 °C with a heating ramp of 10 °C/min⁻¹ in a flow of air.

Raman spectra were obtained on a confocal microprobe laser Raman spectrometer (HORIBA Jobin Yvon) with an excitation laser beam of 532 nm. Spectra in the range of 1000–2000 cm⁻¹ were recorded at room temperature to study the type of deposited coke over the spent catalysts.

2.3. Catalytic Tests

Catalytic tests for CO₂-ODP were carried out in a quartz fixed-bed reactor (6 mm, i.d.) under 550 °C and atmospheric pressure. For each test, 0.25 g of the catalyst (40–60 mesh) diluted with 0.5 g of quartz sand (40–60 mesh) was loaded into the reactor. Firstly, the catalyst was pre-reduced with 20 vol% H₂/He at 500 °C for 1h. After that, the reactor was heated to 550 °C in a He flow, and the gas mixture of Ar/C₃H₈/CO₂/He in a molar ratio of 1/4/4/16 with a total flow rate of 50 mL/min was introduced into the reactor. The products were analyzed by an online gas chromatograph (GC7920, Peking CEAULIGHT) equipped with FID (Porapak Q column) and TCD (TDX-01) detectors. By using Ar as an internal standard, propane and CO₂ conversion, selectivity of different gas products (CH₄, C₂H₄, C₂H₆, and C₃H₆), and propylene yield were calculated by Equations (2)–(5).

$$\text{C}_3\text{H}_8 \text{ conversion} = \frac{[\text{F}_{\text{C}_3\text{H}_8}]_{\text{inlet}} - [\text{F}_{\text{C}_3\text{H}_8}]_{\text{outlet}}}{[\text{F}_{\text{C}_3\text{H}_8}]_{\text{inlet}}} \times 100\% \quad (2)$$

$$\text{CO}_2 \text{ conversion} = \frac{[\text{F}_{\text{CO}_2}]_{\text{inlet}} - [\text{F}_{\text{CO}_2}]_{\text{outlet}}}{[\text{F}_{\text{CO}_2}]_{\text{inlet}}} \times 100\% \quad (3)$$

$$\text{Selectivity of products } i = \frac{n_i \times [\text{F}_i]_{\text{outlet}}}{3 \times ([\text{F}_{\text{C}_3\text{H}_8}]_{\text{inlet}} - [\text{F}_{\text{C}_3\text{H}_8}]_{\text{outlet}})} \times 100\% \quad (4)$$

$$\text{C}_3\text{H}_6 \text{ yield} = \frac{[\text{F}_{\text{C}_3\text{H}_6}]_{\text{outlet}}}{[\text{F}_{\text{C}_3\text{H}_8}]_{\text{inlet}}} \times 100\% \quad (5)$$

The carbon balances calculated from Equation (6) were very close to 100% (98.5 ± 1.5%) for all of the experiments (Figure S1), and thus, the C₃H₈-based selectivity of CO, i.e., CO

produced from C_3H_8 , was calculated by subtracting the sum of the hydrocarbon products ($CH_4 + C_2H_4 + C_2H_6 + C_3H_6$) from 100% with Equation (7).

$$\text{Carbon balance} = \frac{\sum_i n_i \times [F_i]_{\text{outlet}} + 3 \times [F_{C_3H_8}]_{\text{outlet}} + [F_{CO}]_{\text{outlet}} + [F_{CO_2}]_{\text{outlet}}}{3 \times [F_{C_3H_8}]_{\text{inlet}} + [F_{CO_2}]_{\text{inlet}}} \times 100\% \quad (6)$$

$$\text{CO selectivity} = \left(1 - \sum_i \frac{n_i \times [F_i]_{\text{outlet}}}{3 \times ([F_{C_3H_8}]_{\text{inlet}} - [F_{C_3H_8}]_{\text{outlet}})} \right) \times 100\% \quad (7)$$

where, $F_{C_3H_8}$, F_{CO_2} , and F_{CO} are the volumetric flow rate (mL/min) of C_3H_8 , CO_2 , and CO , respectively; i stands for the detected hydrocarbon product, i.e., CH_4 , C_2H_6 , C_2H_4 , and C_3H_6 ; and F_i and n_i represent the flow rate and carbon number of the hydrocarbon product, respectively.

3. Results

3.1. Catalytic Results of CO_2 -ODP

The time-on-stream (TOS) results of CO_2 -ODP over PtSn/SiO₂, PtCe/SiO₂, and PtSnCe/SiO₂ are shown in Figure 1. Indeed, PtSn/SiO₂ showed a very low propane conversion of 4.4% at a TOS of 5 min (Figure 1a). In contrast, a significantly higher propane conversion was achieved over the Ce-containing catalysts, and PtSnCe/SiO₂ showed the highest initial propane conversion of 55.8%. Taking the activity as the propane conversion at a TOS of 5 min, an increased order of PtSn/SiO₂ < PtCe/SiO₂ << PtSnCe/SiO₂ was observed. Moreover, the blank experimental results of CO_2 -ODP indicate a propane conversion of less than 2.5% over SnCe/SiO₂ (Figure S2). Thus, the Pt species over the catalysts are responsible for converting propane, the activity of which is associated with the added SnO₂ and/or CeO₂. Where the initial activity indexed by the CO_2 conversion at a TOS of 5 min (Figure 1b) was concerned, PtSn/SiO₂ showed negligible activity. In contrast, a significantly high initial CO_2 conversion of 26.4% over PtCe/SiO₂ and 25.9% over PtSnCe/SiO₂ was achieved. In the case of stability, Figure 1a,b clearly shows that PtSnCe/SiO₂ was the most stable catalyst at a TOS of 80 min, leading to the concurrently decreased conversions of propane and CO_2 in the same order of PtSnCe/SiO₂ > PtCe/SiO₂ >> PtSn/SiO₂ with increasing TOS.

Concerning product distribution, propylene selectivity was varied to a relatively large extent over these catalysts (Figure 1c). In the case of PtSn/SiO₂, the lowest propylene selectivity of 30.9% was observed at a TOS of 5 min. On the contrary, a higher propylene selectivity was achieved over the Ce-containing catalysts, and the highest initial propylene selectivity of 89.1% was reached over PtSnCe/SiO₂. With increasing TOS, propylene selectivity at the end of the reaction was decreased in the order of PtSnCe/SiO₂ (93.4%) >> PtCe/SiO₂ (45.0%) > PtSn/SiO₂ (27.4%). To understand the side reactions, the selectivity of gaseous byproducts originating from C_3H_8 were examined, and the results are shown in Figure 1d and Figure S3. In the case of PtSnCe/SiO₂ and PtCe/SiO₂, CO was the predominant byproduct, while the selectivity of C_2H_6 , C_2H_4 , and CH_4 was very low. This indicates that CO_2 -RP may be the main side reaction over these catalysts in comparison with cracking [13,28]. The significantly higher CO selectivity of 56.9% at a TOS of 5 min was observed over PtCe/SiO₂, indicating the more favorable breaking of C-C bonds in propane. In contrast, PtSnCe/SiO₂ showed a very low CO selectivity of about 10%, coinciding with the significantly high propylene selectivity. Concerning PtSn/SiO₂, although the calculated selectivity of CO was 53.9% at a TOS of 5 min, supporting the occurrence of CO_2 -RP, its error may be large due to the very low CO_2 conversion (Figure 1b). Thus, the CO selectivity of PtSn/SiO₂ is not further discussed with that of PtSnCe/SiO₂ and PtCe/SiO₂.

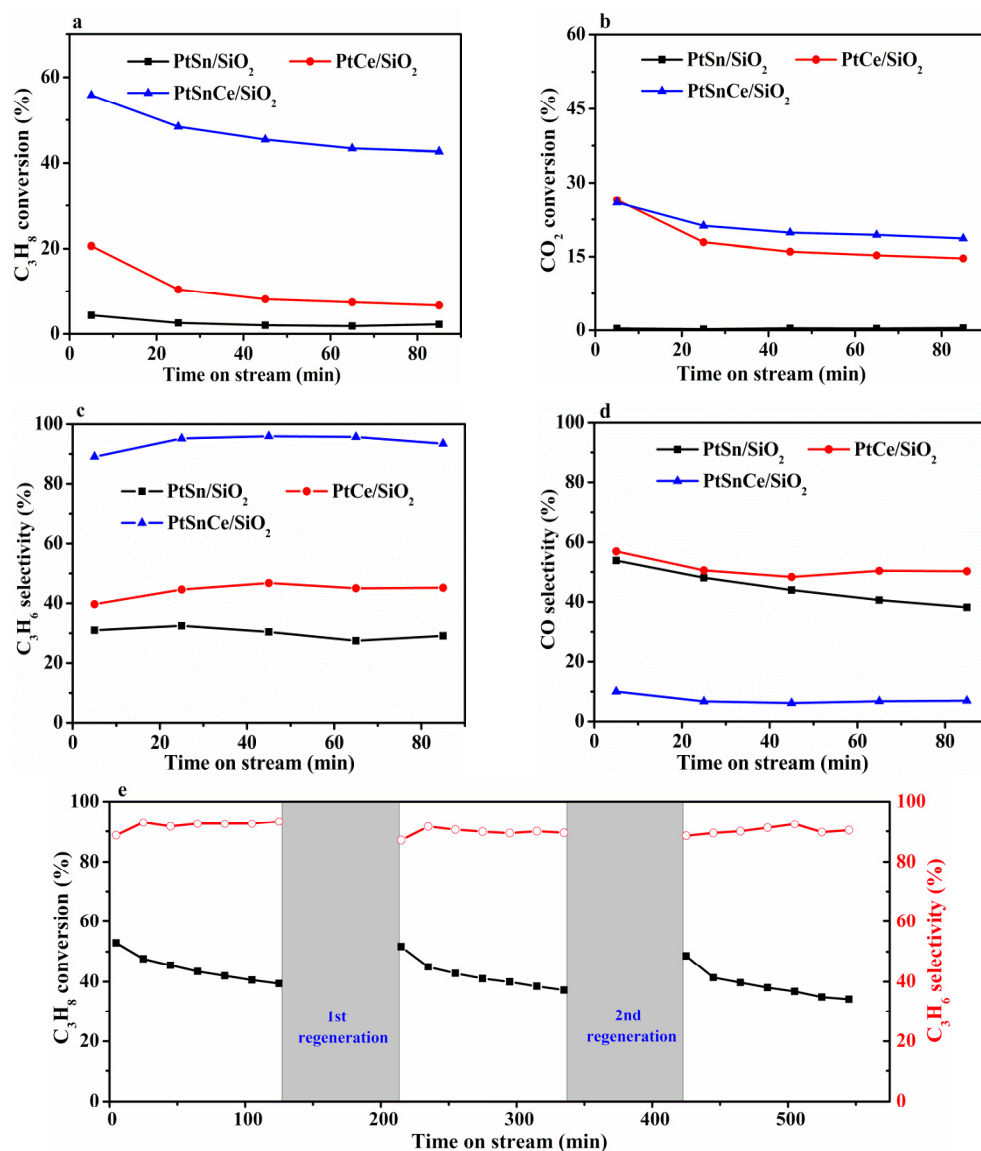


Figure 1. Time-on-stream conversions of C₃H₈ (a) and CO₂ (b); C₃H₆ selectivity (c) and CO selectivity (d) for CO₂-ODP catalyzed by PtSn/SiO₂, PtCe/SiO₂, and PtSnCe/SiO₂; and time-on-stream C₃H₈ conversions/C₃H₆ selectivity over the regenerated PtSnCe/SiO₂ (e) under the conditions of T = 550 °C, Ar/C₃H₈/CO₂/He molar ratio = 1/4/4/16, total flow rate = 50 mL/min, and GHSV = 12,000 mL·g⁻¹·h⁻¹ (conditions for the regeneration: T = 500 °C, air flow = 30 mL/min, t = 30 min).

To show the superior performance of the PtSnCe/SiO₂ catalyst for CO₂-ODP, the calculated space-time yield of propylene (STY_{C₃H₆}) over PtSnCe/SiO₂ and those over different types of catalysts with the best performance from the representative literature are summarized in Table S1. Among the reported catalysts, including CrO_x, VO_x, GaO_x, Pd, and Pt, the highest STY_{C₃H₆} of 0.63 g(C₃H₆)·g(catalyst)⁻¹·h⁻¹ was observed at a reaction temperature of 600 °C over CrO_x-doped mesoporous silica spheres (7.07Cr/MSS-2). In our case, however, the PtSnCe/SiO₂ catalyst showed an initial STY_{C₃H₆} as high as 1.75 g(C₃H₆)·g(catalyst)⁻¹·h⁻¹ at a reaction temperature of 550 °C, which is significantly higher than those over the reported catalysts. Moreover, 1.16 g(C₃H₆)·g(catalyst)⁻¹·h⁻¹ was still achieved, even at a TOS of 6 h, indicating a superior catalytic stability. The durability of PtSnCe/SiO₂ was further investigated by the reaction/regeneration cycles, the regeneration of which is performed at 500 °C in an air flow for 30 min. As shown in Figure 1e, the CO₂-ODP performance of the catalyst regenerated for two times was very

similar to that of the fresh catalyst, indicating the good durability of PtSnCe/SiO₂. Thus, the catalytic results clearly reflect the superiority of the PtSnCe/SiO₂ catalyst for CO₂-ODP.

3.2. Textural and Structural Properties

The N₂ adsorption-desorption isotherms of PtSn/SiO₂, PtCe/SiO₂, and PtSnCe/SiO₂ are shown in Figure S4a. According to the IUPAC classification, all of the catalysts exhibited a similar type-IV isotherm, indicating the presence of mesopores. Moreover, the appearance of an H1-type hysteresis loop over these catalysts occurred at $p/p_0 = 0.4\text{--}0.6$ characterizing the uniform spherical pores. These observations were more directly reflected from the PSD patterns determined by the BJH method. As indicated by Figure S4b, a very narrow and sharp PSD peak at about 3 nm was observed for all of these catalysts. From the calculated textural parameters summarized in Table 1, the BET specific surface area was slightly decreased from 568.9 to 527.3 m²/g in the order of PtSn/SiO₂ > PtCe/SiO₂ > PtSnCe/SiO₂. In the cases of mean pore size and total pore volume, the changes were also very limited. These results suggest very similar textural properties of the samples due to the minimal loadings of Pt, Sn, and/or Ce species over the same silica support.

Table 1. Textural properties, crystallite size, and metal dispersion of the different catalysts.

Catalyst	Specific Surface Area (m ² /g)	Mean Pore Size (nm)	Total Pore Volume (cm ³ /g)	Crystallite Size (nm)		Metal Dispersion *** (%)
				Pt *	CeO ₂ **	
PtSn/SiO ₂	568.9	3.19	0.42	8.5 ± 0.2	-	13.4
PtCe/SiO ₂	536.4	3.25	0.43	3.4 ± 0.2	5.9	20.9
PtSnCe/SiO ₂	527.3	3.16	0.41	2.1 ± 0.3	5.6	41.3

*: The average size of 100 particles randomly selected in the TEM images was measured using Nano Measurer 1.2.5 software. **: calculated from Scherrer's equation and the (111) diffraction of the cubic CeO₂, as given in the XRD patterns. ***: calculated from Equation (1) in Section 2.2 and the H₂-O₂ titration results.

XRD patterns of the catalysts are shown in Figure 2. All of the catalysts exhibited a broad XRD peak at ~22.6°, corresponding to the amorphous nature of the SiO₂ support [29]. In the case of PtSn/SiO₂, the characteristic diffractions at 2θ of 39.8, 46.2, and 67.4° were clearly observed, which were assigned to (111), (200), and (220) crystal planes of the cubic Pt metal, respectively [30,31]. In contrast, when CeO₂ was present, the XRD peaks ascribed to Pt metal disappeared, and only the characteristic diffractions at 2θ of 28.5, 33.1, 47.5, and 56.3° conclusively attributed to the (111), (200), (220), and (311) crystal planes of the cubic fluorite structure of CeO₂, respectively [22,32], were clearly observed over PtCe/SiO₂ and PtSnCe/SiO₂. This indicates that the addition of Ce can significantly improve the dispersion of Pt metal, and the SnO₂ species is present as the amorphous or highly dispersed nature.

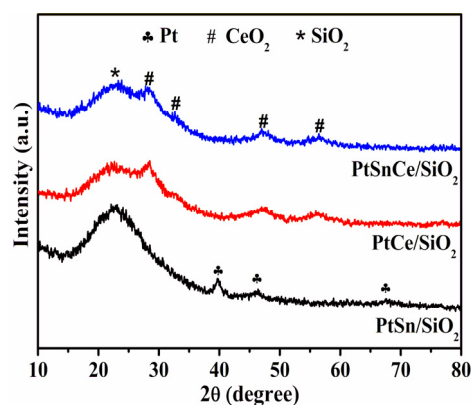


Figure 2. XRD patterns of the PtSn/SiO₂, PtCe/SiO₂, and PtSnCe/SiO₂ catalysts.

To directly observe the Pt particles, the catalysts pre-reduced in 10 vol% H₂/Ar at 500 °C for 1 h were investigated by TEM analysis. As shown in Figure 3a, Pt particles were

clearly observed over all of the catalysts. PtSn/SiO₂ showed the largest Pt particles, while the significantly smaller Pt particles were present over PtCe/SiO₂ and PtSnCe/SiO₂, which supports the XRD results. To make a quantitative comparison, statistics analysis was performed; the Pt particle-size distribution histograms are given in Figure 3b, and the average diameter of Pt is summarized in Table 1. The metallic Pt size was continuously decreased from 8.5 ± 0.2 to 2.1 ± 0.3 nm in the order of PtSn/SiO₂ >> PtCe/SiO₂ > PtSnCe/SiO₂, indicating that the addition of CeO₂ can significantly improve the dispersion of Pt metal. This is further supported by the H₂-O₂ titration results, in which the calculated Pt dispersion was continuously increased from 13.4 to 41.3% in the order of PtSn/SiO₂ < PtCe/SiO₂ < PtSnCe/SiO₂ (Table 1). Generally, the addition of SnO₂ can effectively improve the Pt dispersion. However, this is contradictory to the observations over PtSn/SiO₂, in which a Pt size as high as 8.5 ± 0.2 nm was observed. As for the reason, it has been reported that PtSn/SiO₂ catalysts directly calcined in an oxidative atmosphere during the preparation process show poor Pt dispersion [33] due to the weak interaction between Pt and SnO₂ on the SiO₂ support. This is in agreement with our experimental results, in which all of the catalysts were obtained by calcining in air at 500 °C after impregnation, as described in Section 2.1. In contrast, when CeO₂ was introduced, the Pt size was significantly decreased over PtCe/SiO₂ and PtSnCe/SiO₂. Taking these results into account, the lower Pt size of 2.1 nm for PtSnCe/SiO₂, compared to that of PtCe/SiO₂, indicates that in addition to increasing the Pt dispersion, the presence of CeO₂ can improve the interaction between Pt and SnO₂, leading to the highest Pt dispersion over PtSnCe/SiO₂.

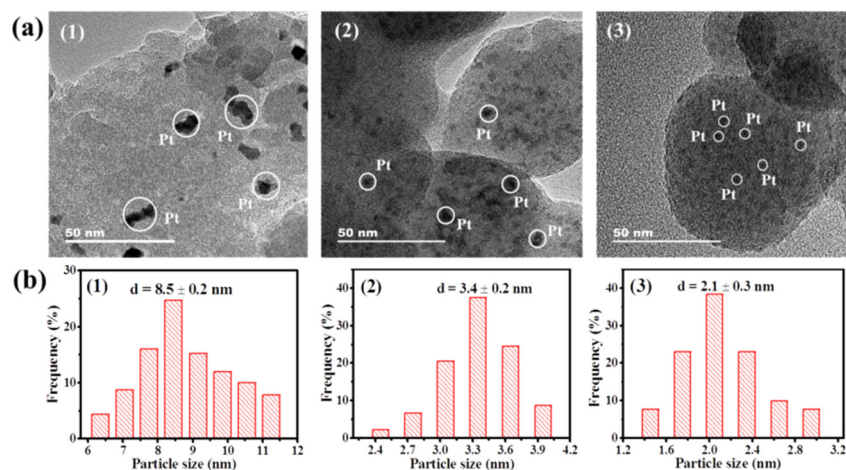


Figure 3. TEM images (a) and size distributions of Pt particles (b) for the reduced catalysts of PtSn/SiO₂ (1), PtCe/SiO₂ (2), and PtSnCe/SiO₂ (3).

3.3. Reduction Behavior

The redox properties of the catalysts were analyzed by H₂-TPR. As shown in Figure 4, for the PtSn/SiO₂ catalyst, a weak and broad reduction peak was observed at ~450 °C, which can be attributed to the reduction of SnO₂ [34,35]. In the case of PtCe/SiO₂, two reduction peaks were observed at 279 °C and 733 °C. The first peak at 279 °C was attributed to the reduction of active oxygen species over the CeO₂ surface, while the very weak peak at 733 °C corresponded to the reduction of the lattice oxygen over the bulk CeO₂ [22,36]. Concerning PtSnCe/SiO₂, only one reduction peak was observed at 233 °C, attributed to the reduction of surface oxygen species. The reduction-peak temperature below 600 °C was continuously decreased in the order of PtSn/SiO₂ >> PtCe/SiO₂ > PtSnCe/SiO₂, while the amount of the H₂ consumption calculated from the reduction peak during H₂-TPR below 600 °C (Table 2) was increased in the order of PtSn/SiO₂ << PtCe/SiO₂ < PtSnCe/SiO₂, leading to the greatest reducibility of PtSnCe/SiO₂. It has been reported that the hydrogen spillover effect induced from the interaction between the Pt and SnO₂/CeO₂ can accelerate the reduction of oxygen over the catalyst, and a higher dispersion of Pt commonly leads to a greater reducibility [37,38]. Based on this explana-

tion, the H₂-TPR results were well understood when the dispersion of Pt, as discussed in Section 3.2, was taken into account. As a result of the highest Pt dispersion over PtSnCe/SiO₂, the reduction of oxides over the catalysts was enhanced due to the strongest hydrogen spillover effect, leading to the lowest reduction-peak temperature and the greatest amount of H₂ consumption.

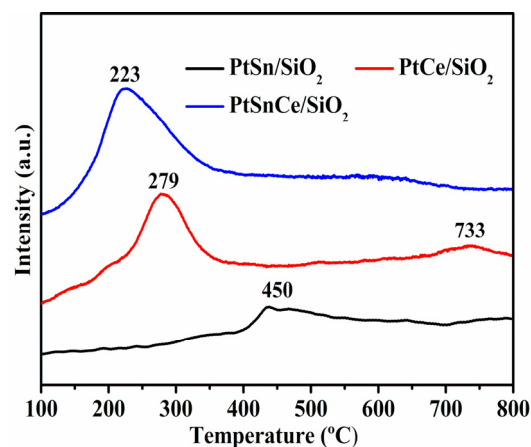


Figure 4. H₂-TPR profiles of the PtSn/SiO₂, PtCe/SiO₂, and PtSnCe/SiO₂ catalysts.

Table 2. H₂ consumption during H₂-TPR below 600 °C and XPS peak-fitting results of different catalysts.

Catalyst	H ₂ Consumption (mol/g)	Pt ⁰ (%)	Pt ²⁺ (%)	Sn ⁰ (%)	Ce ³⁺ (%)
PtSn/SiO ₂	23.5	100.0	0	0	-
PtCe/SiO ₂	78.5	30.5	69.5	-	31.9
PtSnCe/SiO ₂	140.6	33.1	66.9	12.0	43.2

3.4. Chemical States

XPS analysis was used to study the surface chemical states of the catalysts. Before measurements, all of the catalysts were pre-reduced in 10 vol% H₂/Ar at 500 °C for 1 h. Ce 3d spectra are usually fitted with eight Gaussian-Lorentzian peaks corresponding to two pairs of spin-orbit doubles [32,39]. As shown in Figure S5, the peaks labeled as v, v'', v''' and u, u'', u''' were assigned to the ionization of Ce⁴⁺ 3d_{5/2} and Ce⁴⁺ 3d_{3/2}, respectively, while the peaks marked with v' and u' were originated from Ce³⁺ 3d_{5/2} and Ce³⁺ 3d_{3/2}, respectively. Based on those peak areas, the relative content of Ce³⁺ was calculated, defined as the ratio of Ce³⁺/(Ce³⁺ + Ce⁴⁺). As shown in Table 2, the relative content of Ce³⁺ over PtSnCe/SiO₂ is clearly higher than that of PtCe/SiO₂, indicating the formation of more oxygen defects after the reduction. This is consistent with the significantly greater amount of H₂ consumption during the H₂-TPR over the fresh PtSnCe/SiO₂ than that over PtCe/SiO₂ (Table 2), resulting from the stronger hydrogen spillover effect due to the greater dispersion of Pt (Table 1).

As shown in Figure 5a, the binding energies at around 71.4 eV for 4f_{7/2} and 74.7 eV for 4f_{5/2} were clearly observed over PtSn/SiO₂, indicating the presence of metallic Pt⁰ [40]. In contrast, when CeO₂ was added, the binding energies of Pt 4f were clearly increased, and the XPS peaks at 72.8 eV for 4f_{7/2} and 76.1 eV for 4f_{5/2} assigned to Pt²⁺ species [40] were clearly observed over PtCe/SiO₂ and PtSnCe/SiO₂. Following the results of deconvolution of the Pt 4f peaks (Figure 5a), the relative content of Pt⁰ and Pt²⁺ was calculated by respective peak area. As shown in Table 2, PtSn/SiO₂ showed the exclusively metallic Pt species, which is consistent with XRD results (Figure 2). Contrarily, the relative content of Pt²⁺ was as high as 69.5% and 66.9% for PtCe/SiO₂ and PtSnCe/SiO₂, respectively. According to references [41,42], the presence of Pt²⁺ over the CeO₂-containing catalysts originates from the strong interaction between Pt and CeO₂, which may be the key reason for the greater dispersion of Pt over PtCe/SiO₂ and PtSnCe/SiO₂ than over PtSn/SiO₂.

This is supported by the TEM and H₂-O₂ titration results (Figure 3 and Table 1). As shown in Figure 5b, the Sn 3d_{5/2} at about 487.0 eV was deconvoluted to analyze the chemical state of Sn. In the case of PtSn/SiO₂, a symmetric Sn 3d_{5/2} XPS peak with a binding energy of 487.2 eV was observed, indicating the presence of only SnO_x species, as reported in [28]. However, besides oxide species, a small amount of Sn⁰ species located at 485.7 eV was observed over PtSnCe/SiO₂. As for the reason, it is noteworthy that PtSnCe/SiO₂ showed a slightly higher content of Pt⁰ than PtCe/SiO₂ (Table 2), which may originate from the improved interaction between SnO₂ and Pt due to the presence of CeO₂. This coincides well with the presence of Sn⁰ species, indicating the possible formation of Pt-Sn bimetallic nanoparticles [28,43].

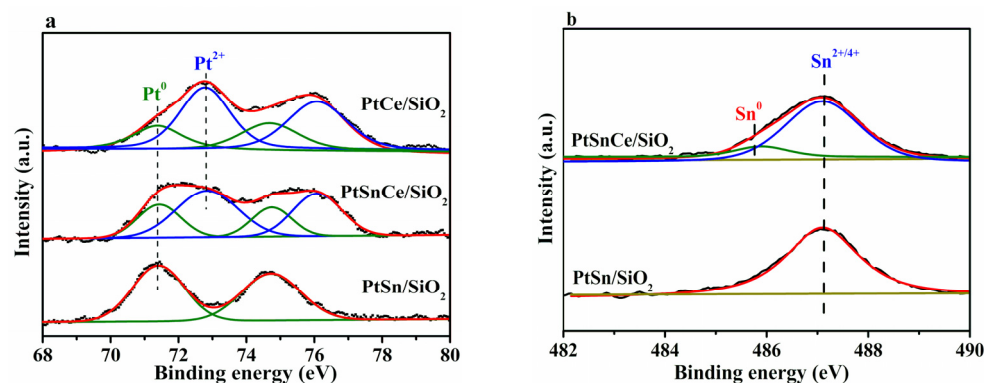


Figure 5. Pt 4f (a) and Sn 3d (b) XPS spectra of the reduced catalysts.

3.5. CO-DRIFTS Studies

To further investigate the structural and electronic properties of Pt, DRIFTS experiments were performed by using CO as a probing molecule since its adsorption on Pt surfaces has been well studied. As shown in Figure 6, two overlapping bands were clearly observed in the case of PtSn/SiO₂ at 2000 and 2024 cm⁻¹, assigned to Si-H stretching vibrations in the different SiO₂ configuration [44]. Moreover, a very weak peak was detected at about 2074 cm⁻¹, assigned to the linearly bonded CO on Pt⁰ terraces, indicating the presence of large, highly coordinated nanoparticles [45,46]. When PtCe/SiO₂ and PtSnCe/SiO₂ were considered, significantly weakened and even disappeared peaks were observed for the Si-H stretching vibrations, which may be due to the coverage of CeO₂ on the SiO₂ surface. Moreover, strong band was observed at ~2060 cm⁻¹, ascribed to the linearly bonded CO on Pt⁰, with intermediate coordination sites, such as edges or steps sites [47], indicating the high dispersion of Pt over these two Ce-containing catalysts [48,49]. This is supported by the results of TEM and H₂-O₂ titration (Figure 3 and Table 1). Noteworthy, besides the band at 2060 cm⁻¹, a weak adsorption band was detected over PtCe/SiO₂ at 1820 cm⁻¹, ascribed to the bridge-bonded CO on two neighboring Pt atoms [24]. However, it disappeared in the case of PtSnCe/SiO₂, accompanying a decreased intensity of the linear adsorption peak at 2060 cm⁻¹. The disappeared bridge-bonded CO over PtSnCe/SiO₂ suggests that the SnO₂ breaks the ensemble of Pt atoms and forms a checkerboard Pt-Sn surface structure [24,50] because CO does not adsorb at the bridge sites between Sn and Pt. The decreased intensity of the peak at 2060 cm⁻¹, in comparison with PtCe/SiO₂, can be explained as the reduced surface coverage of CO due to the presence of SnO₂ [51]. These results indicate that the presence of CeO₂ on a PtSn/SiO₂ catalyst can not only improve the Pt dispersion but also improve the interaction between Pt and SnO₂.

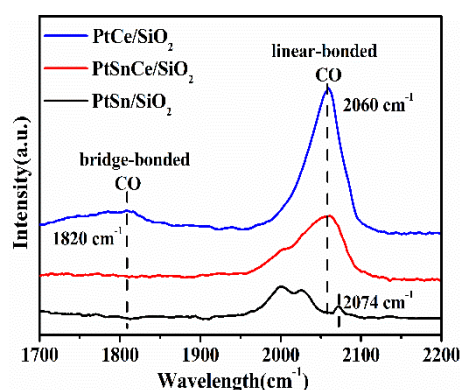


Figure 6. DRIFT spectra of CO adsorption on the reduced catalysts.

4. Discussion

4.1. Key Factors of Catalytic Activity

As indicated by the results in Sections 3.1 and 3.2, the initial C_3H_8 conversion at a TOS of 5 min was increased in the order of $PtSnCe/SiO_2 \gg PtCe/SiO_2 \gg PtSn/SiO_2$, coinciding well with the dispersion of Pt over the catalysts. This indicates that the amount of active Pt species is the key factor determining the activation of propane in the course of CO_2 -ODP, which is consistent with the reported results for PDH [52]. When the activation of CO_2 was considered, the significant conversion of CO_2 was only observed over the Ce-containing catalysts of $PtSnCe/SiO_2$ and $PtCe/SiO_2$, while CO_2 conversion for $PtSn/SiO_2$ was negligible. This indicates that the introduced CeO_2 plays a key role in the activation of CO_2 , which is supported by our previous work for oxidative dehydrogenation of ethylbenzene with CO_2 [53]. To shed some light on these observations, C_3H_8 - and CO_2 -TPD experiments were performed over the catalysts. In the case of C_3H_8 -TPD (Figure 7a), a very broad curve was observed for all of the catalysts in the temperature range of 100–400 °C, indicating the varied strength of adsorbed propane [54,55]. For $PtSn/SiO_2$, two overlapping peaks were clearly observed at about 118 °C and 236 °C, respectively. When $PtCe/SiO_2$ and $PtSnCe/SiO_2$ were considered, the peak maxima were shifted toward higher temperatures in comparison with those of $PtSn/SiO_2$. Moreover, the peak areas of desorbed propane were significantly increased. This indicates the intensified adsorption of propane over the Ce-containing catalysts. The amount of desorbed propane was calculated below 400 °C during C_3H_8 -TPD, and the results are given in Table 3. It was increased in the order of $PtSn/SiO_2 \ll PtCe/SiO_2 < PtSnCe/SiO_2$, which coincides well with the propane conversion. This clearly reveals that the amount of adsorbed propane plays a key role in determining the activity of these catalysts for CO_2 -ODP, which can be reasonably associated with Pt dispersion. As for the adsorption of CO_2 , a broad CO_2 -TPD pattern similar to that of C_3H_8 -TPD was obtained for all of the catalysts (Figure 7b). For $PtSn/SiO_2$, only a small peak was observed at about 126 °C, indicating the very weak adsorption of CO_2 , which is consistent with references [56,57]. In contrast, the peak temperature of desorbed CO_2 increased to 141 °C over $PtCe/SiO_2$ and $PtSnCe/SiO_2$. Moreover, a shoulder peak could be observed at a higher temperature of 242 °C, which can be explained by the stronger adsorbed CO_2 on the surface of CeO_2 . This indicates the presence of CeO_2 -enhanced CO_2 adsorption. As shown in Table 3, the amount of desorbed CO_2 was calculated below 400 °C during CO_2 -TPD. It was increased in the order of $PtSn/SiO_2 \ll PtCe/SiO_2 < PtSnCe/SiO_2$, the changing pattern of which coincides well with that of CO_2 conversion at the steady state of TOS (Figure 1b). It has been reported that CeO_2 with richer oxygen defects commonly leads to enhanced adsorption and activation of CO_2 [21,32]. Following this understanding, the greater amount of adsorbed CO_2 in the case of $PtSnCe/SiO_2$ than that of $PtCe/SiO_2$ can be reasonably ascribed to the presence of more oxygen defects of CeO_2 , as revealed by the Ce 3d XPS results (Table 2). These results indicate that the amount of adsorbed CO_2 plays a

key role in determining the activation of CO₂ over the catalysts, which can be connected with the introduced CeO₂.

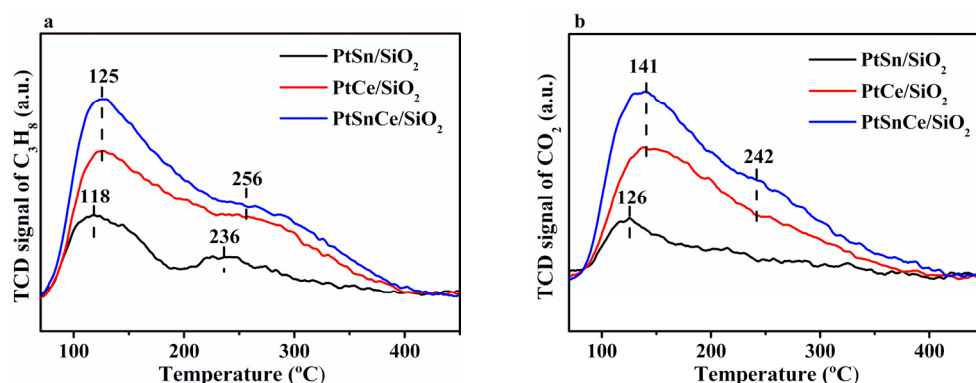


Figure 7. C₃H₈ (a) and CO₂-TPD (b) profiles over the reduced catalysts.

Table 3. Calculated results of C₃H₈-, CO₂-, and C₃H₆-TPD and the coking property of different catalysts.

Catalyst	C ₃ H ₈	CO ₂	C ₃ H ₆	Coke Content (wt%)	I _D /I _G	Coking Rate (g/mol)
	(mmol/g) *					
PtSn/SiO ₂	0.09	0.04	0.10	-	-	-
PtCe/SiO ₂	0.22	0.11	0.23	1.71	0.73	2.09
PtSnCe/SiO ₂	0.30	0.14	0.26	2.53	0.81	0.07

*: Amounts of desorbed C₃H₈, CO₂, and C₃H₆ were determined from the TPD patterns given in Figures 6 and 7.

4.2. Insights into Product Selectivity

As indicated by the results in Section 3.1, the selectivity of propylene varied to a relatively large extent over the PtSn/SiO₂, PtCe/SiO₂, and PtSnCe/SiO₂ catalysts (Figure 1c). According to the analysis of product distribution (Figure 1d), this is explained by the simultaneous occurrence of CO₂-RP in the course of CO₂-ODP. By correlating the characterization results of Sections 3.2–3.5, the significant propylene selectivity over PtSnCe/SiO₂ can be explained as the Ce promoted interaction between Sn and Pt, which favors the breaking of C-H bonds in propane [23,58]. However, in addition to the side reaction of CO₂-RP induced from propane, the selectivity of propylene is also determined by its possible secondary reactions, including successive polymerization (coke deposition) and further cracking, owing to the difficult desorption of propylene from the surface of catalysts [59]. For further insight, C₃H₆-TPD experiments were performed, and the results are given in Figure 8. A very broad desorption signal was observed in the temperature range of 100 to 450 °C for all of the catalysts, indicating the varied strength of propylene adsorption on the surface of the catalyst [54]. In the case of PtSn/SiO₂, two overlapping peaks were observed at about 123 °C and 204 °C. In contrast, both the peak temperature and amount of desorbed propylene over PtCe/SiO₂ and PtSnCe/SiO₂ were clearly higher than over PtSn/SiO₂, indicating a stronger adsorption of propylene. Furthermore, as given in Table 3, the amount of adsorbed propylene was calculated below 450 °C during C₃H₆-TPD and was found to increase in the order of PtSn/SiO₂ << PtCe/SiO₂ < PtSnCe/SiO₂. When propylene selectivity is compared with the amount of propylene adsorption, exactly the same trend is found, i.e., the greater the amount of propylene adsorption, the higher the propylene selectivity. This result is contradictory to the common expectation. Considering the dominant byproduct of CO in the course of CO₂-ODP (Figure 1d), it can be concluded that the simultaneous occurrence of CO₂-RP plays a key role in determining the propylene selectivity in comparison with the secondary reaction of propylene.

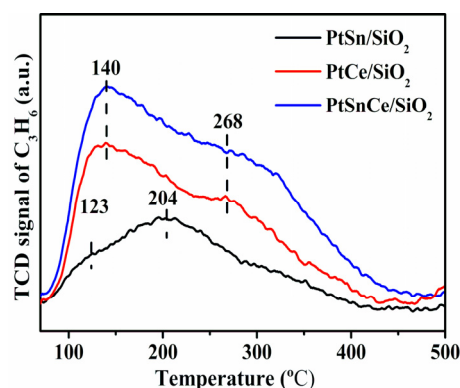


Figure 8. C_3H_6 -TPD profiles of the reduced catalysts.

As a matter of fact, coke deposition on the surface of catalysts is a common issue in the course of CO_2 -ODP, the behavior of which is associated with its catalytic performance [4,54]. TG-DSC was performed to analyze the amount and kind of deposited coke over the spent catalysts after a TOS of 2 h, and the results are shown in Figure S6 and Table 3. For all of the catalysts, a clear weight loss was observed at about 30–200 °C, induced from the physical desorption of water (Figure S6a), accompanying the clearly endothermic peak of DSC curves at around 74 °C (Figure S6b). With a further increase in temperature from 200 to 800 °C, the TG signal commonly assigned to the burning of deposited coke was almost steady in the case of PtSn/SiO₂, indicating a negligible amount of coke formed on the surface. This coincides well with the significantly low propane conversion (Figure 1a). Contrary to this, a weight loss of 1.71% and 2.53% was clearly observed over PtCe/SiO₂ and PtSnCe/SiO₂, respectively, at about 300–600 °C, ascribed to the burning of coke. This was further revealed by the exothermic peak of DSC curves. Moreover, the peak temperature of DSC for PtSnCe/SiO₂ (400 °C) was clearly lower than that for PtCe/SiO₂ (452 °C), suggesting a difference in the degree of graphitization of the deposited coke. To further confirm this, visible Raman characterization was performed. As given in Figure S7, typical Raman shifts were observed over PtCe/SiO₂ and PtSnCe/SiO₂ at 1340 and 1600 cm^{-1} , assigned to the disordered (D band) and graphitic carbon (G band), respectively. To quantify the extent of graphitization of the deposited coke, the intensity ratio of the D and G bands, i.e., I_D/I_G , was calculated. As shown in Table 3, PtSnCe/SiO₂ showed a higher value of I_D/I_G (0.81) than PtCe/SiO₂ (0.73), indicating a lesser extent of graphitization of coke species [32]. This is in agreement with the DSC results (Figure S6b). The difference in the species of deposited coke can be explained by the fact that PtCe/SiO₂ is favorable to CO_2 -RP, while PtSnCe/SiO₂ is promising for CO_2 -ODP. The lesser extent of graphitization of coke species on the surface of PtSnCe/SiO₂ mainly originated from the polymerization of the produced C_3H_6 . However, PtCe/SiO₂ led to the formation of more graphitic carbon species due to the severe breaking of the C-C bond in propane through CO_2 -RP. The coking rate (g/mol) of PtCe/SiO₂ and PtSnCe/SiO₂, defined as grams of deposited coke, was calculated following references [54,60] by converting 1 mole of propane after a TOS of 2 h. In the case of PtSnCe/SiO₂, the coking rate was 0.07 g/mol, which is clearly lower than that of PtCe/SiO₂ (2.09 g/mol). This indicates that coke deposition over PtSnCe/SiO₂ is significantly inhibited, which may result from the lesser extent of graphitization of coke species for CO_2 -ODP.

5. Conclusions

In summary, a highly efficient CO_2 -ODP catalyst was developed with $STY_{C_3H_6}$ as high as $1.75 \text{ g}(C_3H_6) \cdot \text{g}(\text{catalyst})^{-1} \cdot \text{h}^{-1}$ by simply impregnating Ce (6 wt%) into PtSn/SiO₂. Moreover, CO_2 -ODP performance was essentially restored after the regeneration of the catalyst at 500 °C for 30 min in an air flow. Additionally, the promotional effect of CeO₂ on PtSn/SiO₂ played a key role in determining the initial CO_2 -ODP performance, leading to the same increased order of PtSn/SiO₂ < PtCe/SiO₂ < PtSnCe/SiO₂ for the initial propane

conversion of 4.4%, 20.6%, and 55.8% and propylene selectivity of 31.0%, 39.7%, and 89.1%. Physical, chemical, and spectra characterizations reveal that the addition of CeO₂ led to an increased Pt dispersion of 13.4% for PtSn/SiO₂ < 20.9% for PtCe/SiO₂ < 41.3% for PtSnCe/SiO₂ and strong interactions between Pt and Sn species over the PtSnCe/SiO₂ catalyst, which favors the synchronized activation of C-H bonds in propane and the C=O bonds in CO₂ molecules. This was explained as the enhanced adsorption of propane and CO₂ in the order of PtSn/SiO₂ < PtCe/SiO₂ < PtSnCe/SiO₂, essentially originated from the rich oxygen defects over the added CeO₂. With these understandings, the modification of catalysts with improved oxygen defects over oxides, as well as the search for promoters with richer oxygen defects than CeO₂, is expected to produce a more effective Pt-based catalyst for CO₂-ODP, with additional studies still in progress in our laboratory.

Supplementary Materials: The following supporting information can be downloaded at: <https://www.mdpi.com/article/10.3390/nano12030417/s1>. Figure S1: Carbon balances of CO₂-ODP over the PtSn/SiO₂, PtCe/SiO₂, and PtSnCe/SiO₂ catalysts at different times on stream, Figure S2: Time-on-stream catalytic activity for CO₂-ODP over SnCe/SiO₂, Figure S3: Time-on-stream selectivity of CH₄, C₂H₄, and C₂H₆, Figure S4: N₂ adsorption/desorption isotherms and pore-size distributions determined by the BJH method for PtSn/SiO₂, PtCe/SiO₂ and PtSnCe/SiO₂ catalysts, Figure S5: Ce 3d XPS spectra of the reduced PtCe/SiO₂ and PtSnCe/SiO₂ catalysts, Figure S6: TG and DSC patterns of the catalysts after CO₂-ODP for a time on stream of 2 h, Figure S7: Raman spectra of the catalysts after CO₂-ODP for a time on stream of 2 h, Table S1: List of the reaction conditions and the main results of CO₂-ODP over different catalysts [13,16,54,61–68].

Author Contributions: Conceptualization, Z.-W.L.; methodology, L.W. and G.-Q.Y.; validation, Z.-W.L., G.-Q.Y. and X.R.; formal analysis, G.-Q.Y. and L.W.; investigation, G.-Q.Y. and X.R.; resources, Z.-W.L.; data curation, L.W.; writing—original draft preparation, L.W.; writing—review and editing, G.-Q.Y. and Z.-W.L.; visualization, G.-Q.Y.; supervision, Z.-W.L.; project administration, Z.-W.L.; funding acquisition, Z.-W.L. All authors have read and agreed to the published version of the manuscript.

Funding: This work was supported by the National Natural Science Foundation of China (grant number 21636006) and the Fundamental Research Funds for the Central Universities (grant number GK201901001).

Institutional Review Board Statement: Not applicable.

Informed Consent Statement: Not applicable.

Data Availability Statement: The data presented in this study are available on request from the corresponding author.

Conflicts of Interest: The authors declare no conflict of interest.

References

1. Amghizar, I.; Vandewalle, L.A.; Van, K.M.; Marin, G.B. New trends in olefin production. *Engineering* **2017**, *3*, 171–178. [[CrossRef](#)]
2. Galvis, H.M.T.; Jong, K.P. Catalysts for production of lower olefins from synthesis gas: A review. *ACS Catal.* **2013**, *3*, 2130–2149. [[CrossRef](#)]
3. Sattler, J.J.; Ruiz-Martinez, J.; Santillan-Jimenez, E.; Weckhuysen, B.M. Catalytic dehydrogenation of light alkanes on metals and metal oxides. *Chem. Rev.* **2014**, *114*, 10613–10653. [[CrossRef](#)] [[PubMed](#)]
4. Atanga, M.A.; Rezaei, F.; Jawad, A.; Fitch, M.; Rownaghi, A.A. Oxidative dehydrogenation of propane to propylene with carbon dioxide. *Appl. Catal. B* **2018**, *220*, 429–445. [[CrossRef](#)]
5. Zhang, L.; Wang, Z.-Y.; Song, J.; Lang, Y.; Chen, J.-G.; Luo, Q.-X.; He, Z.-H.; Wang, K.; Liu, Z.-W.; Liu, Z.-T. Facile synthesis of SiO₂ supported GaN as an active catalyst for CO₂ enhanced dehydrogenation of propane. *J. CO₂ Util.* **2020**, *38*, 306–313. [[CrossRef](#)]
6. Jiang, X.; Sharma, L.; Fung, V.; Park, S.J.; Jones, C.W.; Sumpter, B.G.; Baltrusaitis, J.; Wu, Z. Oxidative dehydrogenation of propane to propylene with soft oxidants via heterogeneous catalysis. *ACS Catal.* **2021**, *11*, 2182–2234. [[CrossRef](#)]
7. Chen, S.; Zeng, L.; Mu, R.; Xiong, C.; Zhao, Z.J.; Zhao, C.; Pei, C.; Peng, L.; Luo, J.; Fan, L.S.; et al. Modulating lattice oxygen in dual-functional Mo-V-O mixed oxides for chemical looping oxidative dehydrogenation. *J. Am. Chem. Soc.* **2019**, *141*, 18653–18657. [[CrossRef](#)]
8. Li, G.; Liu, C.; Cui, X.; Yang, Y.; Shi, F. Oxidative dehydrogenation of light alkanes with carbon dioxide. *Green Chem.* **2021**, *23*, 689. [[CrossRef](#)]

9. Carrero, C.A.; Schloegl, R.; Wachs, I.E.; Schomaecker, R. Critical literature review of the kinetics for the oxidative dehydrogenation of propane over well-defined supported vanadium oxide catalysts. *ACS Catal.* **2014**, *4*, 3357–3380. [[CrossRef](#)]
10. Wang, S.; Zhu, Z.H. Catalytic conversion of alkanes to olefins by carbon dioxide oxidative dehydrogenations—A review. *Energy Fuel* **2004**, *18*, 1126–1139. [[CrossRef](#)]
11. Wegrzyniak, A.; Jarczewski, S.; Wegrzynowicz, A.; Michorczyk, B.; Kustrowski, P.; Michorczyk, P. Catalytic behavior of chromium oxide supported on nanocasting-prepared mesoporous alumina in dehydrogenation of propane. *Nanomaterials* **2017**, *7*, 249. [[CrossRef](#)] [[PubMed](#)]
12. Ruthwik, N.; Kavaya, D.; Shadab, A.; Lingaiah, N.; Sumana, C. Thermodynamic analysis of chemical looping combustion integrated oxidative dehydrogenation of propane to propylene with CO₂. *Chem. Eng. Process.* **2020**, *153*, 107959. [[CrossRef](#)]
13. Gomez, E.; Kattel, S.; Yan, B.; Yao, S.; Liu, P.; Chen, J.G. Combining CO₂ reduction with propane oxidative dehydrogenation over bimetallic catalysts. *Nat. Commun.* **2018**, *9*, 1398. [[CrossRef](#)] [[PubMed](#)]
14. Ascoop, I.; Galvita, V.V.; Alexopoulos, K.; Reyniers, M.-F.; Voort, P.V.D.; Bliznuk, V.; Marin, G.B. The role of CO₂ in the dehydrogenation of propane over WO_x-VO_x/SiO₂. *J. Catal.* **2016**, *335*, 1–10. [[CrossRef](#)]
15. Shishido, T.; Shimamura, K.; Teramura, K.; Tanaka, T. Role of CO₂ in dehydrogenation of propane over Cr-based catalysts. *Catal. Today* **2012**, *185*, 151–156. [[CrossRef](#)]
16. Nowicka, E.; Reece, C.; Althahban, S.M.; Mohammed, K.M.H.; Kondrat, S.A.; Morgan, D.J.; He, Q.; Willock, D.J.; Golunski, S.; Kiely, C.J.; et al. Elucidating the role of CO₂ in the soft oxidative dehydrogenation of propane over ceria-based catalysts. *ACS Catal.* **2018**, *8*, 3454–3468. [[CrossRef](#)]
17. Dai, Y.; Gao, X.; Wang, Q.; Wan, X.; Zhou, C.; Yang, Y. Recent progress in heterogeneous metal and metal oxide catalysts for direct dehydrogenation of ethane and propane. *Chem. Rev.* **2021**, *50*, 5590–5630. [[CrossRef](#)]
18. Zhang, J.; Deng, Y.; Cai, X.; Chen, Y.; Peng, M.; Jia, Z.; Jiang, Z.; Ren, P.; Yao, S.; Xie, J.; et al. Tin-assisted fully exposed platinum clusters stabilized on defect-rich graphene for dehydrogenation reaction. *ACS Catal.* **2019**, *9*, 5998–6005. [[CrossRef](#)]
19. Kumar, M.S.; Chen, D.; Holmen, A.; Walmsley, J.C. Dehydrogenation of propane over Pt-SBA-15 and Pt-Sn-SBA-15: Effect of Sn on the dispersion of Pt and catalytic behavior. *Catal. Today* **2009**, *142*, 17–23. [[CrossRef](#)]
20. Chen, S.; Chang, X.; Sun, G.; Zhang, T.; Xu, Y.; Wang, Y.; Pei, C.; Gong, J. Propane dehydrogenation: Catalyst development, new chemistry, and emerging technologies. *Chem. Rev.* **2021**, *50*, 3315–3354. [[CrossRef](#)]
21. Etim, U.J.; Zhang, C.; Zhong, Z. Impacts of the catalyst structures on CO₂ activation on catalyst surfaces. *Nanomaterials* **2021**, *11*, 3265. [[CrossRef](#)]
22. Wang, H.; Yang, G.-Q.; Song, Y.-H.; Liu, Z.-T.; Liu, Z.-W. Defect-rich Ce_{1-x}Zr_xO₂ solid solutions for oxidative dehydrogenation of ethylbenzene with CO₂. *Catal. Today* **2019**, *324*, 39–48. [[CrossRef](#)]
23. Xue, M.; Zhou, Y.; Zhang, Y.; Liu, X.; Duan, Y.; Sheng, X. Effect of cerium addition on catalytic performance of PtSnNa/ZSM-5 catalyst for propane dehydrogenation. *J. Nat. Gas Chem.* **2012**, *21*, 324–331. [[CrossRef](#)]
24. Motagamwala, A.H.; Almallahi, R.; Wortman, J.; Igenegbai, V.O.; Linic, S. Stable and selective catalysts for propane dehydrogenation operating at thermodynamic limit. *Science* **2021**, *373*, 217–222. [[CrossRef](#)] [[PubMed](#)]
25. Sun, Q.; Wang, N.; Fan, Q.; Zeng, L.; Mayoral, A.; Miao, S.; Yang, R.; Jiang, Z.; Zhou, W.; Zhang, J.; et al. Subnanometer bimetallic platinum-zinc clusters in zeolites for propane dehydrogenation. *Angew. Chem. Int. Ed.* **2020**, *59*, 2–11. [[CrossRef](#)]
26. Akhtar, M.; Tompkins, F.C. The hydrogen-oxygen titration on platinum films: Determination of the catalytically active area. *Trans. Faraday Soc.* **1971**, *67*, 2454–2460. [[CrossRef](#)]
27. Wang, T.; Jiang, F.; Liu, G.; Zeng, L.; Zhao, Z.; Gong, J. Effects of Ga doping on Pt/CeO₂-Al₂O₃ catalysts for propane dehydrogenation. *AIChE J.* **2016**, *62*, 4365–4376. [[CrossRef](#)]
28. Lin, C.; Yang, Z.; Pan, H.; Cui, J.; Lv, Z.; Liu, X.; Tian, P.; Xiao, Z.; Li, P.; Xu, J.; et al. Ce-introduced effects on modification of acidity and Pt electronic states on Pt-Sn/ γ -Al₂O₃ catalysts for catalytic reforming. *Appl. Catal. A Gen.* **2021**, *617*, 118116. [[CrossRef](#)]
29. Baek, J.; Yun, H.J.; Yun, D.; Choi, Y.; Yi, J. Preparation of highly dispersed chromium oxide catalysts supported on mesoporous silica for the oxidative dehydrogenation of propane using CO₂: Insight into the nature of catalytically active chromium sites. *ACS Catal.* **2012**, *2*, 1893–1903. [[CrossRef](#)]
30. Deng, L.; Miura, H.; Ohkubo, T.; Shishido, T.; Wang, Z.; Hosokawa, S.; Teramura, K.; Tanaka, T. The importance of direct reduction in the synthesis of highly active Pt-Sn/SBA-15 for n-butane dehydrogenation. *Catal. Sci. Technol.* **2019**, *9*, 947–956. [[CrossRef](#)]
31. Kaneko, S.; Izuka, M.; Takahashi, A.; Ohshima, M.; Kurokawa, H.; Miura, H. Pt dispersion control in Pt/SiO₂ by calcination temperature using chloroplatinic acid as catalyst precursor. *Appl. Catal. A Gen.* **2012**, *427–428*, 85–91. [[CrossRef](#)]
32. Wang, H.; Cao, F.-X.; Song, Y.-H.; Yang, G.-Q.; Ge, H.-Q.; Liu, Z.-T.; Qu, Y.-Q.; Liu, Z.-W. Two-step hydrothermally synthesized Ce_{1-x}Zr_xO₂ for oxidative dehydrogenation of ethylbenzene with carbon dioxide. *J. CO₂ Util.* **2019**, *34*, 99–107. [[CrossRef](#)]
33. Deng, L.; Miura, H.; Shishido, T.; Wang, Z.; Hosokawa, S.; Teramura, K.; Tanaka, T. Elucidating strong metal-support interactions in Pt-Sn/SiO₂ catalyst and its consequences for dehydrogenation of lower alkanes. *J. Catal.* **2018**, *365*, 277–291. [[CrossRef](#)]
34. Huang, L.; Xu, B.; Yang, L.; Fan, Y. Propane dehydrogenation over the PtSn catalyst supported on alumina-modified SBA-15. *Catal. Commun.* **2008**, *9*, 2593–2597. [[CrossRef](#)]
35. Wang, H.; Huang, H.; Bashir, K.; Li, C. Isolated Sn on mesoporous silica as a highly stable and selective catalyst for the propane dehydrogenation. *Appl. Catal. A Gen.* **2020**, *590*, 117291. [[CrossRef](#)]
36. Chen, A.; Zhou, Y.; Ta, N.; Li, Y.; Shen, W. Redox properties and catalytic performance of ceria-zirconia nanorods. *Catal. Sci. Technol.* **2015**, *5*, 4184–4192. [[CrossRef](#)]

37. Zhang, H.; Wang, J.; Zhang, Y.; Jiao, Y.; Ren, C.; Gong, M.; Chen, Y. A study on H₂-TPR of Pt/Ce_{0.27}Zr_{0.73}O₂ and Pt/Ce_{0.27}Zr_{0.70}La_{0.03}O_x for soot oxidation. *Appl. Surf. Sci.* **2016**, *377*, 48–55. [[CrossRef](#)]
38. Lee, J.; Ryou, Y.; Chan, X.; Kim, T.J.; Kim, D.H. How Pt interacts with CeO₂ under the reducing and oxidizing environments at elevated temperature: The origin of improved thermal stability of Pt/CeO₂ compared to CeO₂. *J. Phys. Chem. C* **2016**, *120*, 25870–25879. [[CrossRef](#)]
39. Xiang, X.; Zhao, H.; Yang, J.; Zhao, J.; Yan, L.; Song, H.; Chou, L. Nickel based mesoporous silica-ceria-zirconia composite for carbon dioxide reforming of methane. *Appl. Catal. A Gen.* **2016**, *520*, 140–150. [[CrossRef](#)]
40. Ono, L.K.; Croy, J.R.; Heinrich, H.; Roldan Cuenya, B. Oxygen chemisorption, formation, and thermal stability of Pt oxides on Pt nanoparticles supported on SiO₂/Si(001): Size effects. *J. Phys. Chem. C* **2011**, *115*, 16856–16866. [[CrossRef](#)]
41. Bruix, A.; Lykhach, Y.; Matolínová, I.; Neitzel, A.; Skála, T.; Tsud, N.; Vorokhta, M.; Stetsovych, V.; Ševčíková, K.; Mysliveček, J.; et al. Maximum noble-metal efficiency in catalytic materials: Atomically dispersed surface platinum. *Angew. Chem. Int. Ed.* **2014**, *53*, 10525–10530. [[CrossRef](#)] [[PubMed](#)]
42. Xiong, H.; Lin, S.; Goetze, J.; Pletcher, P.; Guo, H.; Kovarik, L.; Artyushkova, K.; Weckhuysen, B.M.; Datye, A.K. Thermally stable and regenerable platinum-tin clusters for propane dehydrogenation prepared by atom trapping on ceria. *Angew. Chem. Int. Ed.* **2017**, *56*, 8986–8991. [[CrossRef](#)] [[PubMed](#)]
43. Zhu, H.; Anjum, D.H.; Wang, Q.; Abou-Hamad, E.; Emsley, L.; Dong, H.; Laveille, P.; Li, L.; Samal, A.K.; Basset, J.-M. Sn surface-enriched Pt-Sn bimetallic nanoparticles as a selective and stable catalyst for propane dehydrogenation. *J. Catal.* **2014**, *320*, 52–62. [[CrossRef](#)]
44. Xu, H.; Wen, C.; Liu, H.; Li, Z.P.; Shen, W.Z. Relationship of microstructure properties to oxygen impurities in nanocrystalline silicon photovoltaic materials. *J. Appl. Phys.* **2013**, *113*, 093501. [[CrossRef](#)]
45. Balakrishnan, K.; Sachdev, A.; Schwank, J. Chemisorption and FTIR study of bimetallic Pt-Au/SiO₂ catalysts. *J. Catal.* **1990**, *121*, 441–455. [[CrossRef](#)]
46. Podda, N.; Corva, M.; Mohamed, F.; Feng, Z.; Dri, C.; Dvorač, F.; Matolin, V.; Comelli, G.; Peressi, M.; Vesselli, E. Experimental and theoretical investigation of the restructuring process induced by CO at near ambient pressure: Pt nanoclusters on graphene/Ir(111). *ACS Nano* **2016**, *11*, 1041–1053. [[CrossRef](#)]
47. Arteaga, G.J.; Anderson, J.A.; Rochester, C.H. FTIR study of CO adsorption on coked Pt-Sn/Al₂O₃ catalysts. *Catal. Lett.* **1999**, *58*, 189–194. [[CrossRef](#)]
48. Wang, H.-Z.; Zhang, W.; Jiang, J.-W.; Sui, Z.-J.; Zhu, Y.-A.; Ye, G.-H.; Chen, D.; Zhou, X.-G.; Yuan, W.-K. The role of H₂S addition on Pt/Al₂O₃ catalyzed propane dehydrogenation: A mechanistic study. *Catal. Sci. Technol.* **2019**, *9*, 867–876. [[CrossRef](#)]
49. Boccuzzi, F.; Chiorino, A.; Guglielminotti, E. Effects of structural defects and alloying on the FTIR spectra of CO adsorbed on PtZnO. *Surf. Sci.* **1996**, *268*, 264–269. [[CrossRef](#)]
50. Wang, Q.; Tichit, D.; Meunier, F.; Guesmi, H. Combined DRIFTS and DFT study of CO adsorption and segregation modes in Pt-Sn nanoalloys. *J. Phys. Chem. C* **2020**, *124*, 9979–9989. [[CrossRef](#)]
51. Moscu, A.; Schuurman, Y.; Veyre, L.; Thieuleux, C.; Meunier, F. Direct evidence by in situ IR CO monitoring of the formation and the surface segregation of a Pt-Sn alloy. *Chem. Commun.* **2014**, *50*, 8590. [[CrossRef](#)]
52. Zhang, W.; Wang, H.; Jiang, J.; Sui, Z.; Zhu, Y.; Chen, D.; Zhou, X. Size Dependence of Pt catalysts for propane dehydrogenation: From atomically dispersed to nanoparticles. *ACS Catal.* **2020**, *10*, 12932–12942. [[CrossRef](#)]
53. Wang, H.; Zhu, W.; Yang, G.-Q.; Zhang, Y.-W.; Song, Y.-H.; Jiang, N.; Liu, Z.-T.; Liu, Z.-W. Insights into the oxidative dehydrogenation of ethylbenzene with CO₂ catalyzed by the ordered mesoporous V₂O₅-Ce_{0.5}Zr_{0.5}O₂-Al₂O₃. *Ind. Eng. Chem. Res.* **2019**, *58*, 21372–21381. [[CrossRef](#)]
54. Wang, J.; Song, Y.-H.; Liu, Z.-T.; Liu, Z.-W. Active and selective nature of supported CrO_x for the oxidative dehydrogenation of propane with carbon dioxide. *Appl. Catal. B* **2021**, *297*, 120400. [[CrossRef](#)]
55. Hu, Z.-P.; Wang, Y.; Yang, D.; Yuan, Z.-Y. CrO_x supported on high-silica HZSM-5 for propane dehydrogenation. *J. Energy Chem.* **2020**, *47*, 225–233. [[CrossRef](#)]
56. Burri, D.R.; Choi, K.M.; Han, D.S.; Jiang, N.; Burri, A.; Park, S.E. Oxidative dehydrogenation of ethylbenzene to styrene with CO₂ over SnO₂-ZrO₂ mixed oxide nanocomposite catalysts. *Catal. Today* **2008**, *131*, 173–178. [[CrossRef](#)]
57. Choi, H.; Oh, S.; Park, J.Y. High methane selective Pt cluster catalyst supported on Ga₂O₃ for CO₂ hydrogenation. *Catal. Today* **2020**, *352*, 212–219. [[CrossRef](#)]
58. Yu, C.; Ge, Q.; Xu, H.; Li, W. Effects of Ce addition on the Pt-Sn/ γ -Al₂O₃ catalyst for propane dehydrogenation to propylene. *Appl. Catal. A Gen.* **2006**, *315*, 58–67. [[CrossRef](#)]
59. Shi, L.; Deng, G.M.; Li, W.C.; Miao, S.; Wang, Q.N.; Zhang, W.P.; Lu, A.H. Al₂O₃ nanosheets rich in pentacoordinate Al³⁺ ions stabilize Pt-Sn clusters for propane dehydrogenation. *Angew. Chem. Int. Ed.* **2015**, *54*, 13994–13998. [[CrossRef](#)]
60. Yang, G.-Q.; He, Y.-J.; Song, Y.-H.; Wang, J.; Liu, Z.-T.; Liu, Z.-W. Oxidative dehydrogenation of propane with carbon dioxide catalyzed by Zn_xZr_{1-x}O_{2-x} solid solutions. *Ind. Eng. Chem. Res.* **2021**, *60*, 17850–17861. [[CrossRef](#)]
61. Wang, H.-M.; Chen, Y.; Yan, X.; Lang, W.-Z.; Guo, Y.-J. Cr doped mesoporous silica spheres for propane dehydrogenation in the presence of CO₂: Effect of Cr adding time in sol-gel process. *Microporous and Mesoporous Mater.* **2019**, *284*, 69–77. [[CrossRef](#)]
62. Michorczyk, P.; Ogonowski, J.; Zeńczak, K. Activity of chromium oxide deposited on different silica supports in the dehydrogenation of propane with CO₂—A comparative study. *J. Mol. Catal. A Chem.* **2011**, *349*, 1–12. [[CrossRef](#)]

63. Zhang, F.; Wu, R.; Yue, Y.; Yang, W.; Gu, S.; Miao, C.; Hua, W.; Gao, Z. Chromium oxide supported on ZSM-5 as a novel efficient catalyst for dehydrogenation of propane with CO₂. *Microporous and Mesoporous Mater.* **2011**, *145*, 194–199. [[CrossRef](#)]
64. Xue, X.-L.; Lang, W.-Z.; Yan, X.; Guo, Y.J. Dispersed vanadium in three-dimensional dendritic mesoporous silica nanospheres: Active and stable catalysts for the oxidative dehydrogenation of propane in the presence of CO₂. *ACS Appl. Mater. Interfaces* **2017**, *9*, 15408–15423. [[CrossRef](#)] [[PubMed](#)]
65. Wang, Z.-Y.; He, Z.-H.; Xia, Y.; Zhang, L.; Wang, K.; Wang, W.; Yang, Y.; Chen, J.-G.; Liu, Z.-T. Oxidative dehydrogenation of propane to propylene in the presence of CO₂ over gallium nitride supported on NaZSM-5. *Ind. Eng. Chem. Res.* **2021**, *60*, 2807–2817. [[CrossRef](#)]
66. Xiao, H.; Zhang, J.; Wang, P.; Wang, X.; Pang, F.; Zhang, Z.; Tan, Y. Dehydrogenation of propane over a hydrothermal-synthesized Ga₂O₃-Al₂O₃ catalyst in the presence of carbon dioxide. *Catal. Sci. Technol.* **2016**, *6*, 5183–5195. [[CrossRef](#)]
67. Chen, M.; Xu, J.; Cao, Y.; He, H.-Y.; Fan, K.-N.; Zhuang, J.-H. Dehydrogenation of propane over In₂O₃-Al₂O₃ mixed oxide in the presence of carbon dioxide. *J. Catal.* **2010**, *272*, 101–108. [[CrossRef](#)]
68. Ren, Y.; Zhang, F.; Hua, W.; Yue, Y.; Gao, Z. ZnO supported on high silica HZSM-5 as new catalysts for dehydrogenation of propane to propene in the presence of CO₂. *Catal. Today* **2009**, *148*, 316–322. [[CrossRef](#)]